

Interaction models and configurational entropies of binary MoTa and the MoNbTaW high entropy alloy

Andrew D. Kim and Michael Widom 

Department of Physics, Carnegie Mellon University, Pittsburgh, Pennsylvania 15213, USA



(Received 6 December 2022; revised 23 March 2023; accepted 19 May 2023; published 6 June 2023)

We introduce a simplified method to model the interatomic interactions of high entropy alloys based on a lookup table of cluster energies. These interactions are employed in replica exchange Monte Carlo simulations with histogram analysis to obtain thermodynamic properties across a broad temperature range. Kikuchi's cluster variation method entropy formalism is applied to directly calculate entropy from statistics on short- and long-range chemical order, and we discuss the convergence of the entropy as clusters of differing size are included. A high temperature series expansion aids in our understanding of the convergence. Computer codes implementing these methods, and supporting data, are freely available on the internet.

DOI: [10.1103/PhysRevMaterials.7.063803](https://doi.org/10.1103/PhysRevMaterials.7.063803)

I. INTRODUCTION

High entropy alloys (HEAs) are multicomponent solid solutions that randomly distribute chemical species among the sites of a crystal lattice [1,2]. The high configurational entropy arising from random chemical substitution may help to stabilize single phases at elevated temperatures. Substitutional disorder increases the possible composition range of a phase, allowing for the tuning of mechanical or other properties. The possibility to find alloys with favorable properties in previously unexplored compositions has motivated intensive study of equiatomic high entropy and other concentrated alloy systems, with strong recent focus on refractory alloys that exhibit high strength and other useful properties at high temperatures [3–6]. Many excellent reviews survey the recent developments [7–9].

Although the distribution is nominally random, preferences in chemical bonding correlate the chemical identities of nearby atoms, creating short-range chemical order that reduces the entropy below the ideal value of $k_B \ln(N_s)$ for N_s species. In the case of strong bonding preferences or in equilibrium at low temperatures, long-range chemical order and even phase separation may arise [10–12]. The stability of the high entropy solid solution has been discussed through qualitative models [13,14] and simulation [15–17].

Computer simulation provides powerful techniques to predict and quantify chemical order for a given model of interatomic interaction. Models range from accurate, but expensive, first principles methods, through reasonably accurate, but complicated, machine learning and cluster expansion approaches, to simplified empirical formulas such as embedded atom or pair potentials. Here we introduce a simple, but accurate, approach based on a lookup table of precalculated first principles energies. We then apply replica exchange Monte Carlo simulation [18] to reach equilibrium over a broad range of temperatures.

The resulting data set allows us to calculate thermodynamic quantities, including the entropy, through the use of

the multiple histogram method [19,20]. We compare our results with formulas adapted from the cluster variation method [21–23] (CVM) that express the entropy in terms of simulated cluster probabilities and show the convergence of the CVM entropy with respect to the included clusters. The pattern of convergence is interpreted through the use of a high temperature series expansion [24,25] that confirms the sequence of optimal clusters [26]. Because we employ Monte Carlo-simulated cluster probabilities in the CVM formulas [27,28], we obtain the (approximate) entropy without the need for thermodynamic integration.

Our approach is illustrated through application to the widely studied body centered cubic (bcc) refractory MoNbTaW high entropy alloy [3]. This compound is believed to exhibit strong short-range chemical order in equilibrium (although this is difficult to achieve experimentally) due to strong binding of Mo and Ta at nearest neighbors. Our model exhibits the expected Strukturbericht A2 to B2 (Pearson type cI2 to cP2) ordering transition at intermediate temperatures and phase separation at low temperatures [11,29–31]. Finite size variation of the specific heat and susceptibility peaks indicate that the transition is of the three-dimensional (3D) Ising type. We compare the behavior of the four-component HEA with the binary solid solution MoTa, which provides a simpler picture of similar behavior.

II. METHODS

This section describes our interaction model, the replica exchange simulation method, histogram analysis of simulation data, the cluster variation method entropy formulas, and the high temperature series expansion. Several of our codes and other data are available from [32].

A. Interaction model

Each of the four chemical species (Mo, Nb, Ta, and W) individually takes the bcc crystal structure. In combination

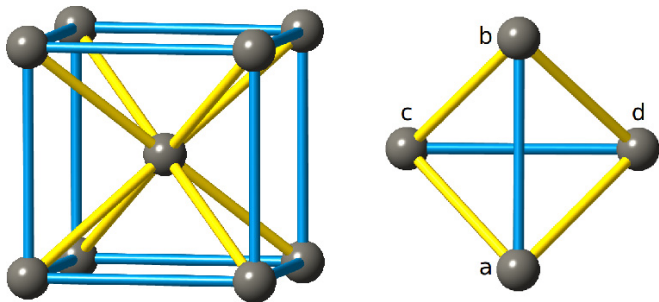


FIG. 1. bcc unit cell (left) and bcc tetrahedron (right). Nearest-neighbor bonds are in yellow and next-nearest-neighbor bonds are in blue. Tetrahedron sites a and b are “even” (cube vertex), while c and d are “odd” (body center) sites.

they occupy sites of the bcc lattice to form a disordered solid solution at high temperatures, but they order and eventually phase separate at low temperatures, all the while maintaining the underlying bcc sites. We are interested in clusters containing nearest- and next-nearest-neighbor pairs, including triangles and the bcc tetrahedron (see Fig. 1). This four-point cluster may be considered the primitive cell of the quaternary Heusler crystal type [33] (Strukturbericht L2₁, Pearson cF16) and hence may be repeated periodically to fill space.

We enumerated the complete set of $4^4 = 256$ arrangements of the four species on the four tetrahedron sites, of which 55 are symmetry inequivalent, and calculated the corresponding Heusler structure energies using density functional theory (DFT). Specifically, we employ VASP [34] with projector augmented wave potentials [35] in the Perdew-Burke-Ernzerhof generalized gradient approximation [36]. The cubic symmetries of the structures prevented atomic relaxation, and we held the lattice parameters fixed at 3.2305 Å, which is representative of both the quaternary and the binary; the precise value has no qualitative impact. Although the individual elements will relax to different volumes, the low lattice distortion of the high entropy alloy [31,37] shows that volume and displacement relaxation effects will be limited, including in its separated low temperature phases.

The resulting energies provide a lookup table (available in Ref. [32]) that can be used to quickly evaluate the energy of any arrangement of the chemical species on bcc lattice sites. To evaluate the total energy, we decompose the structure into its constituent tetrahedra $\{t\}$. Let $\alpha(t)$, $\beta(t)$, $\gamma(t)$, and $\delta(t)$ designate the chemical species at vertices a , b , c , and d , respectively, of tetrahedron t . This tetrahedron contributes energy $E(\alpha, \beta, \gamma, \delta)/24$ per atom to the total energy, where $E(\alpha, \beta, \gamma, \delta)$ is the energy per primitive cell of the four-atom Heusler crystal with species α , β , γ , and δ . An additional factor of 6 arises because the bcc structure has six tetrahedra per atom. The total energy

$$E = \frac{1}{24} \sum_t E(\alpha(t), \beta(t), \gamma(t), \delta(t)), \quad (1)$$

is equivalent in form to the energy model of Refs. [22,23]. It can be reexpressed as

$$E/N = \frac{1}{4} \sum_{\alpha, \beta, \gamma, \delta} E(\alpha, \beta, \gamma, \delta) z_{\alpha\beta\gamma\delta}, \quad (2)$$

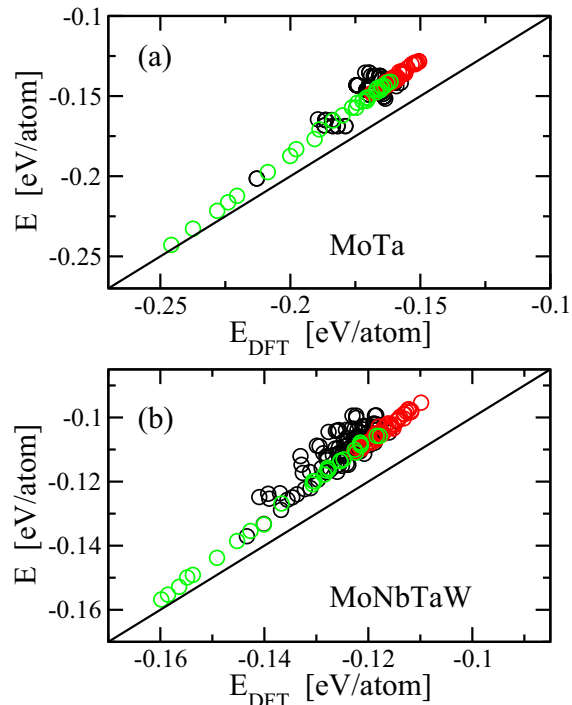


FIG. 2. Parity plot for tetrahedron model energy/atom vs full (unrelaxed) DFT energy/atom for (a) MoTa and (b) MoNbTaW. All structures are equiatomic; black shows random 16-atom structures, red shows random 128-atom structures, and green shows MC-generated 128-atom structures. See the Appendix for a discussion of the skew.

with N being the total number sites and $z_{\alpha\beta\gamma\delta}$ being the frequency of the four-point cluster with species $\alpha\beta\gamma\delta$ normalized to sum to 1. Our energies are calculated relative to the atomic fraction weighted energies of elemental Mo, Nb, Ta, and W, so they represent the energy of formation. We may think of this energy as being analogous to a cluster expansion [38] containing just a single four-point cluster.

To test the accuracy of this model we created parity plots of model energy vs full DFT energy/atom as shown in Fig. 2(a) for equiatomic binary MoTa and Fig. 2(b) for equiatomic quaternary MoNbTaW. The model energies lie close to parity with a mean absolute error of 21 meV/atom for MoTa and 14 meV/atom for MoNbTaW. Crucially, the lowest energy structures lie very close to parity, so we accurately capture the low temperature properties. We observe a systematic skewing of model energy above the parity line and give a heuristic interpretation of its origin in the Appendix.

B. Replica exchange simulation

Replica exchange simulations [18], also known as parallel tempering, aim to accelerate the sampling of configuration space by sharing multiple configurations (replicas) among multiple temperatures in a manner that preserves the properly weighted ensemble at each temperature. When configurations are swapped between temperatures, the diversity of the equilibrium ensemble at each temperature is enriched by the addition of a new independent configuration. From the

perspective of a single configuration, getting swapped to a higher temperature may facilitate its evolution by raising the likelihood of escape from a local energy minimum.

The probability for a configuration C_i of energy E_i to occur in equilibrium at temperature T_i (inverse temperature $\beta_i = 1/k_B T_i$) is $P_i = \exp(\beta_i E_i)/Z(T_i)$, with $Z(T)$ being the partition function for temperature T . The joint probability for a pair of configurations C_i of energy E_i and C_j of energy E_j at respective temperatures T_i and T_j is

$$P(C_i, C_j | T_i, T_j) = e^{-(\beta_i E_i + \beta_j E_j)} / Z(T_i) Z(T_j). \quad (3)$$

The joint probability for C_i to occur at temperature T_j and C_j to occur at temperature T_i is given by the same formula with energies E_i and E_j interchanged. The ratio of probabilities is

$$P(C_i, C_j | T_i, T_j) / P(C_j, C_i | T_i, T_j) = e^{\Delta\beta\Delta E}, \quad (4)$$

with $\Delta\beta = \beta_i - \beta_j$ and $\Delta E = E_i - E_j$. Hence, the equilibrium ensemble probabilities at temperatures T_i and T_j are preserved if the configurations are swapped with the probability given by the ratio in Eq. (4). Note that, conveniently, the partition functions (which are usually unknown in computer simulations) cancel in the ratio.

In addition to replica swaps we must evolve the configurations at each temperature. We apply a Monte Carlo process to attempt discrete swaps of chemical species. Equilibrium at temperature T is maintained if the attempts are accepted with probability $\exp(-\Delta E/k_B T)$, with ΔE being the energy change created by the swap. Recall that the swapped configurations are appropriately weighted members of the ensembles at their new temperatures—no minimum period of annealing following a swap is required, so the duration of conventional Monte Carlo can be chosen at liberty.

Figure 3(a) illustrates a portion of the time evolution of thermostat temperatures. Each configuration is represented by a different color. Temperatures are spaced so that potential energy distributions of adjacent temperatures overlap sufficiently [see Fig. 3(b)] to achieve temperature swap probabilities of 20% or greater. Data collection began following lengthy preannealing during which energy and order parameter distributions relaxed to steady states. By calculating averages and fluctuations of energy at each temperature, we obtain the energy and specific heat at the simulated temperatures. We also gather statistics on the frequencies of occurrence $z_{\alpha\beta\gamma\delta}$ for tetrahedra with chemical species $\alpha\beta\gamma\delta$ that we need for our CVM entropy calculations.

C. Histogram analysis

The probability that any configuration has energy E in equilibrium at temperature T is $P(E) = \Omega(E) \exp(-\beta E) / Z(T)$, where $\Omega(E)$ is the configurational density of states. If we knew $\Omega(E)$, we could evaluate the partition function

$$Z(T) = \int dE \Omega(E) e^{-E/k_B T} \quad (5)$$

and could then obtain the free energy as $F = -k_B T \ln Z$. Given $F(T)$, we may obtain the internal energy $U = -\partial(\beta F) / \partial\beta$, entropy $S = (U - F) / T$, and the specific heat as $c = \partial U / \partial T = -T \partial^2 U / \partial T^2$.

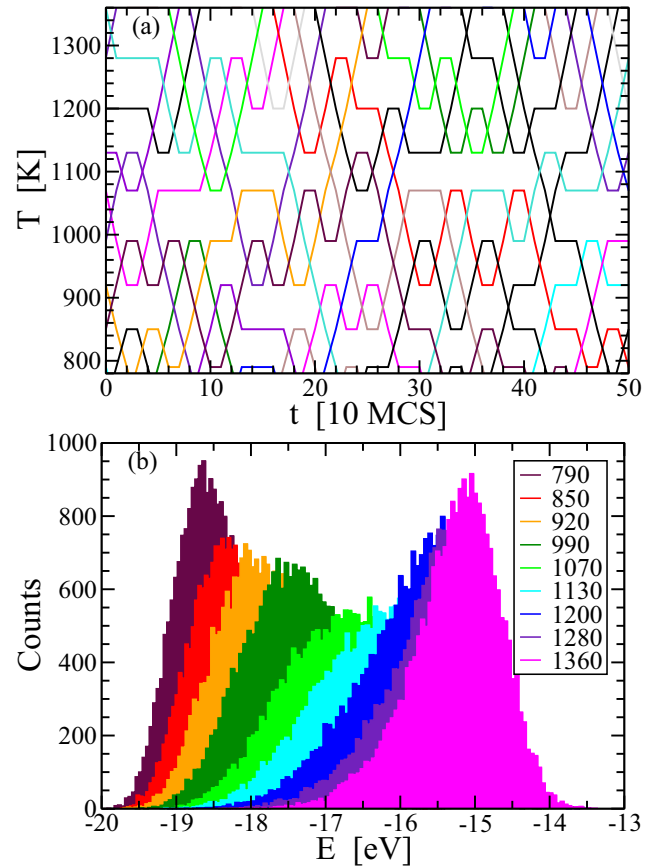


FIG. 3. Illustration of the quaternary MoNbTaW replica exchange simulation in an $L \times L \times L$ supercell with $L = 4$. (a) $T(t)$ graph illustrating the replica exchange. Each color represents the time evolution of a single initial configuration whose temperature is repeatedly swapped with its neighbors; (b) energy histograms at selected temperatures.

During a simulation at temperature T the frequency with which energy E occurs is proportional to the density of states $\Omega(E)$ times the Boltzmann factor $\exp(-\beta E) / Z(T)$. Hence, we may express the density of states as [19]

$$\Omega_T(E) \equiv H_T(E) e^{\beta E}, \quad (6)$$

where the subscript T on the histogram $H_T(E)$ reminds us that the density of states $\Omega_T(E)$ is an approximation obtained from a simulation at temperature T and that it differs from the true Ω by an unknown constant factor that is equivalent to setting the zero of entropy. Substituting Ω_T into Eq. (5) and taking the logarithm, we can evaluate the free energy $F(T')$ as a continuously varying function of temperature T' . The unknown constant factor in Ω_T results in an unknown additive constant in $\beta' F(T')$. This does not impact the internal energy U or specific heat c , but it shifts the entropy S by a uniform constant. The derivatives to obtain U , S , and c may be taken analytically (holding Ω constant), and their values also become continuously varying functions of T' .

The free energy $F(T')$ is most accurate for T' in the vicinity of the simulated temperature T because the histogram is best resolved over the range of highly probable energies. Luckily, the method generalizes to include

multiple histograms accumulated at different temperatures T , with [20,39]

$$\Omega(E) = \frac{\sum_T H_T(E)}{\sum_T e^{(F(T)-E)/k_B T}}. \quad (7)$$

The free energies $F(T)$ must be obtained self-consistently with $\Omega(E)$. Starting with an arbitrary $F(T)$, we obtain Ω from Eq. (7) and then an improved estimate of $F(T)$ through Eq. (5). We iterate this procedure until F has sufficiently converged. In this manner the relative free energy can be extended across the entire range of simulated temperatures.

D. CVM

We exploit the formalism of Kikuchi's cluster variation method to define a hierarchy of approximate entropy models based on the sequence of single-, two-, three-, and, ultimately, four-point cluster frequencies. Starting with the four-point frequencies $z_{\alpha\beta\gamma\delta}$ already introduced in Eq. (2), we define three-point frequencies $u_{\alpha\gamma\delta}$, $u_{\beta\gamma\delta}$, $u_{\alpha\beta\gamma}$, and $u_{\alpha\beta\delta}$ by summing $z_{\alpha\beta\gamma\delta}$ over one of its four indices. Similarly, we introduce pairs for nearest neighbors, $y_{\alpha\gamma}$, $y_{\alpha\delta}$, $y_{\beta\gamma}$, and $y_{\beta\delta}$; next-nearest neighbors $v_{\alpha\beta}$ and $v_{\gamma\delta}$; and points x_α , x_β , x_γ , and x_δ .

The entropy associated with a given cluster Γ is $\Sigma(\Gamma) = -\sum \Gamma \ln \Gamma$, where the sum is over the cluster variables. For example,

$$\Sigma(x_\alpha) = -\sum_\alpha x_\alpha \ln x_\alpha. \quad (8)$$

We also introduce shorthand notation $\Sigma(X) = [\Sigma(x_\alpha) + \Sigma(x_\beta) + \Sigma(x_\gamma) + \Sigma(x_\delta)]/4$, $\Sigma(Y) = [\Sigma(y_{\alpha\gamma}) + \Sigma(y_{\alpha\delta}) + \Sigma(y_{\beta\gamma}) + \Sigma(y_{\beta\delta})]/4$, $\Sigma(V) = [\Sigma(v_{\alpha\beta}) + \Sigma(v_{\gamma\delta})]/2$, $\Sigma(U) = [\Sigma(u_{\alpha\gamma\delta}) + \Sigma(u_{\beta\gamma\delta}) + \Sigma(u_{\alpha\beta\gamma}) + \Sigma(u_{\alpha\beta\delta})]/4$, and $\Sigma(Z) = \Sigma(z_{\alpha\beta\gamma\delta})$. As discussed in [17,22,33,40,41], we build up higher approximations to the entropy through inclusion of entropy-reducing information contained in successively larger

clusters, while correcting for the overcounting of subclusters. Specifically, we obtain (in units of k_B)

$$\begin{aligned} S_{\text{Point}} &= \Sigma(X), \\ S_{\text{NN}} &= -7 \Sigma(X) + 4 \Sigma(Y), \\ S_{\text{NNN}} &= -13 \Sigma(X) + 4 \Sigma(Y) + 3 \Sigma(V), \\ S_{\text{Tri}} &= 23 \Sigma(X) - 20 \Sigma(V) - 9 \Sigma(Y) + 12 \Sigma(U), \\ S_{\text{Tetra}} &= -\Sigma(X) + 4 \Sigma(Y) + 3 \Sigma(V) - 12 \Sigma(U) + 6 \Sigma(Z). \end{aligned} \quad (9)$$

Coefficients of the highest order cluster equal the numbers of such clusters per site, while the lower order coefficients reflect the systematic exclusion of subclusters. For example, S_{Point} is the Bragg-Williams ideal mixing entropy [42], while S_{NN} reduces S_{Point} by the mutual information contained in the nearest-neighbor cluster frequencies [33].

Usually, in the CVM, the cluster frequencies are derived by minimizing the free energy $E - TS$. Since we already have cluster frequencies in hand from our simulation, we simply substitute their values into Eq.(9).

E. High T expansion

In order to model the convergence of the CVM entropy with respect to maximum cluster size in Eq. (9), we carry out a high temperature series expansion [24,25] of the cluster frequencies and apply the CVM formalism to these series. For our purpose it suffices to consider the Ising model, $H = J \sum_{\langle ij \rangle} \sigma_i \sigma_j$. Here J is the nearest-neighbor coupling constant, and $\sigma_i = \pm 1$ is the spin at site $i = a - d$ [see Fig. 1(b) for site labels]. We could consider this to be a model for binary MoTa, in which the spin value denotes chemical species and a negative value of J would favor bonding of unlike species. To evaluate Eq. (9) we need cluster frequencies up to four-point $z_{\sigma_a \sigma_b \sigma_c \sigma_d}$ expanded up to fourth order in $t \equiv \tanh(J/k_B T)$,

$$\begin{aligned} z_{\sigma_a \sigma_b \sigma_c \sigma_d} &= \frac{1}{Z} \cosh^{4N}(J/k_B T) 2^{N-4} \{1 + t(\sigma_a \sigma_c + \sigma_b \sigma_c + \sigma_a \sigma_d + \sigma_b \sigma_d) + t^2[4(\sigma_a \sigma_c + \sigma_b \sigma_d) + 2\sigma_a \sigma_b \sigma_c \sigma_d] \\ &\quad + t^3 12(\sigma_a \sigma_c + \sigma_b \sigma_c + \sigma_a \sigma_d + \sigma_b \sigma_d) + t^4[12N + 56(\sigma_a \sigma_b + \sigma_c \sigma_d) + 12\sigma_a \sigma_b \sigma_c \sigma_d] + \dots\}. \end{aligned} \quad (10)$$

Fewer-point cluster frequencies are obtained by summing over spins, including the partition function itself,

$$Z = \sum_{\sigma_a \sigma_b \sigma_c \sigma_d} Z z_{\sigma_a \sigma_b \sigma_c \sigma_d} \quad (11)$$

$$= \cosh^{4N}(J/k_B T) 2^{N-4} (1 + 12Nt^4 + \dots). \quad (12)$$

Setting the free energy $F = -k_B T \ln Z$ and expanding in powers of $1/T$, we obtain entropy per site

$$S/k_B = \ln 2 - 2 \left(\frac{J}{k_B T} \right)^2 - 35 \left(\frac{J}{k_B T} \right)^4 + \dots \quad (13)$$

The cluster frequencies and the entropy are exact up to fourth order in $J/k_B T$ and consistent with prior results [43,44].

Inserting the cluster frequencies obtained from the expansion (10) into the CVM formulas, we obtain the following expansions for the entropy (in units of k_B):

$$S_{\text{NN}} = \ln 2 - 2 \left(\frac{J}{k_B T} \right)^2 - 47 \left(\frac{J}{k_B T} \right)^4 + \dots, \quad (14)$$

$$S_{\text{NNN}} = \ln 2 - 2 \left(\frac{J}{k_B T} \right)^2 - 79 \left(\frac{J}{k_B T} \right)^4 + \dots, \quad (15)$$

$$S_{\text{Tri}} = \ln 2 - 2 \left(\frac{J}{k_B T} \right)^2 - 29 \left(\frac{J}{k_B T} \right)^4 + \dots, \quad (16)$$

$$S_{\text{Tetra}} = \ln 2 - 2 \left(\frac{J}{k_B T} \right)^2 - 35 \left(\frac{J}{k_B T} \right)^4 + \dots \quad (17)$$

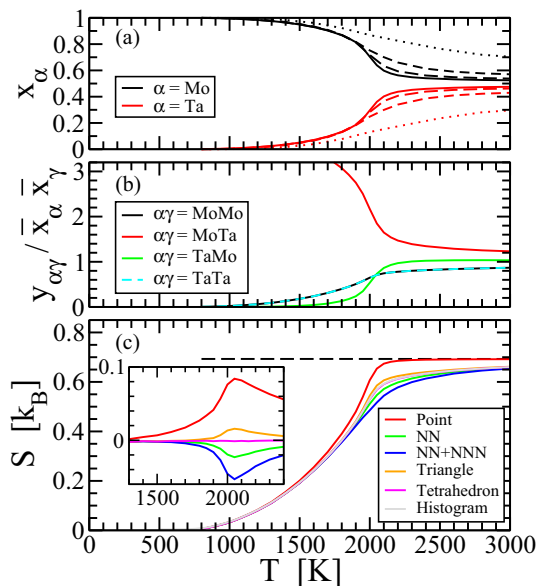


FIG. 4. Binary MoTa of size $L = 8$ (1024 atoms). (a) Occupation x_α of even sites a and b (dotted, short-dashed, and long-dashed lines are for sizes 2, 4, and 6, respectively). (b) ac site pair frequencies $y_{\alpha\gamma}$ normalized by global mean concentrations \bar{x}_α and \bar{x}_γ . (c) Simulated histogram and CVM-predicted entropies (inset: residuals to the histogram). The dashed line shows $S/k_B = \ln 2$.

Notice that we obtain the correct quadratic term already using simply the nearest-neighbor (NN) frequencies $y_{\alpha\gamma}$. However, the quartic term is too large in magnitude, so that the NN approximation underestimates the entropy as temperature drops. This overcorrection is due to the presence of closed loops of NN bonds causing the same information to be counted multiple times [45,46]. For example, the correlation propagated from a to d passing through c and b augments the direct correlation of a with d [see Fig. 1(b)]. Including the next-nearest-neighbor (NNN) term makes the problem worse because we are subtracting the mutual information between a and b yet again. Inclusion of the Tri term overcompensates and, consequently, overestimates the entropy, while, finally, inclusion of the Tetra term restores the proper quartic coefficient. In summary, NN pairs yields entropies that are exact up to second order in the inverse temperature, while Tetra clusters are required to achieve improved accuracy.

III. RESULTS

A. MoTa

Figure 4(a) plots the temperature-dependent a site occupation x_α over the range from 800 K up to the approximate melting temperature of 3000 K. We adopt a convention where we shift the simulated structure so that the maximum Mo occupation occurs on the “even” sublattice (site classes a and b). Evidently, a transition to long-range order occurs in the vicinity of $T_c \approx 2020$ K, with x_α converging towards the global mean concentration $\bar{x}_\alpha = 1/2$ above T_c but diverging away below. Even above T_c the NN pair frequencies $y_{\alpha\gamma}$ deviate from the independent expectation $x_\alpha x_\gamma$, as shown in

Fig. 4(b), with an enhanced frequency of MoTa pairs. The discrepancy grows rapidly below T_c .

Notice that a slight bias of order $1/\sqrt{N}$ artificially raises x_{Mo} relative to x_{Ta} , even above T_c , due to fluctuations for finite system sizes N . The bias grows in the vicinity of T_c due to diverging fluctuations at the phase transition. The same bias causes y_{MoTa} to differ slightly from y_{TaMo} above T_c . The identity $y_{\text{MoMo}} = y_{\text{TaTa}}$ is forced by the equality of $\bar{x}_\alpha = \bar{x}_\gamma$.

CVM cluster-based estimates of entropy and our histogram values are shown in Fig. 4(c). Because of the unknown partition function discussed in Sec. II C, the histogram method yields only relative entropy, so we adjust it to match the CVM tetrahedron value at 3000 K. The fact that it vanishes at low temperature indicates the histogram values should be accurate across the full temperature range. Even above T_c , where sublattice occupations remain equal, the deviations of cluster frequencies from independence cause the entropy to fall below its ideal mixing value of $k_B \ln 2$. The entropy loss accelerates below T_c , and the net entropy tends towards zero for all of our CVM estimates.

The inset shows entropy residuals relative to the histogram method. Note that the point values undercorrect the ideal mixing, while the pair value overcorrects it and the two-pair value strongly overcorrects it. As seen in our discussion of the high temperature series (Sec. II E), this can be attributed to the cumulative effect of correlations extending around closed loops. The deviations are maximal around T_c , supporting the role of longer-range correlations. The triangle approximation undercorrects, while the tetrahedron values lie close to the multiple histogram at all temperatures. Our high temperature series expansions reproduce each of those details of convergence of approximations at temperatures above T_c , notably the qualitative improvement upon including the Tetra term. As the CVM is a generalized mean field theory [46], the errors are maximal around T_c , then fall off again as temperature drops.

Owing to the finite sizes of our simulated systems, all thermodynamic functions vary smoothly. To confirm the presence of a genuine thermodynamic phase transition, we must examine their system size dependence. We plot the specific heat and generalized susceptibility in Fig. 5. The generalized susceptibility is defined as

$$\chi = \frac{N}{k_B T} (\langle M^2 \rangle - \langle M \rangle^2), \quad (18)$$

where we define $M = x_{\text{Mo}} - x_{\text{Ta}}$ on the even sites. Divergences in c and χ reveal thermodynamic singularities. In order to determine the character of the phase transition, we apply standard methods of finite size scaling [47] and plot the scaled specific heat $c/L^{\alpha/\nu}$ and the scaled susceptibility $\chi/L^{\gamma/\nu}$ as a function of the scaled reduced temperature $t = L^{1/\nu}(T - T_c)/T_c$ in the insets. We set T_c as the peak susceptibility temperature for $L = 8$, and we take the established 3D Ising values of the critical exponents [48], $\alpha = 0.110$, $\gamma = 1.2372$, and $\nu = 0.6301$. The convergence towards common scaled functions indicates the transition is in the Ising class, as expected for a binary alloy.

The low temperature phase takes the CsCl structure (Strukturbericht type B2, Pearson cP2). The actual ground state according to full first principles calculations [11] is Pearson type oC12, which is locally B2 with periodic antiphase faults;

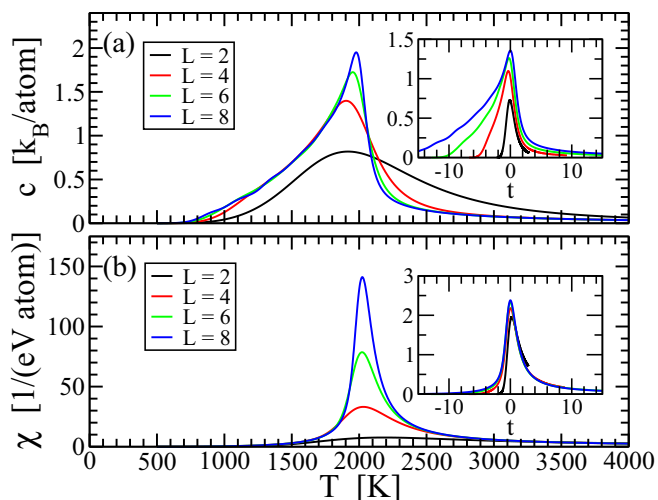


FIG. 5. Binary MoTa. (a) Specific heat $c(T)$ and (b) susceptibility $\chi(T)$ vs temperature T for system sizes $L = 2$ (black), 4 (red), 6 (green), and 8 (blue). Insets show scaling functions as defined in text.

the B2 phase lies above oC12 by just 1 meV/atom. A total of 10 distinct ordered phases are predicted at varying compositions, all based on an underlying bcc lattice. Experimentally, only a solid solution is reported, with no ordered phases.

B. MoNbTaW

The MoNbTaW quaternary behaves similarly to the MoTa binary. As seen in Fig. 6, the dominant ordering occurs between Mo and Ta on the even and odd sites, respectively. The Nb occupation and correlations generally follow Ta, and W generally follows Mo, as previously seen [11]. Likewise, the

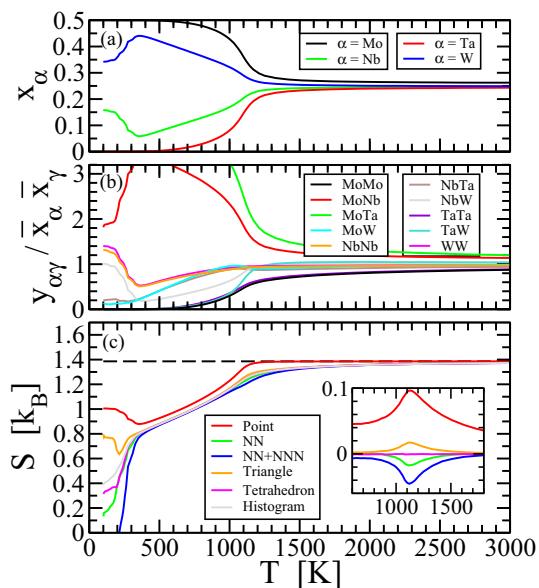


FIG. 6. Quaternary MoNbTaW of size $L = 8$ (1024 atoms). (a) Occupation x_α of the a site. (b) ac site pair frequencies $y_{\alpha\gamma}$ normalized by global mean concentrations \bar{x}_α and \bar{x}_γ . (c) Simulated histogram and CVM-predicted entropies (inset: residuals with respect to the histogram). The dashed line shows $S/k_B = \ln 4$.

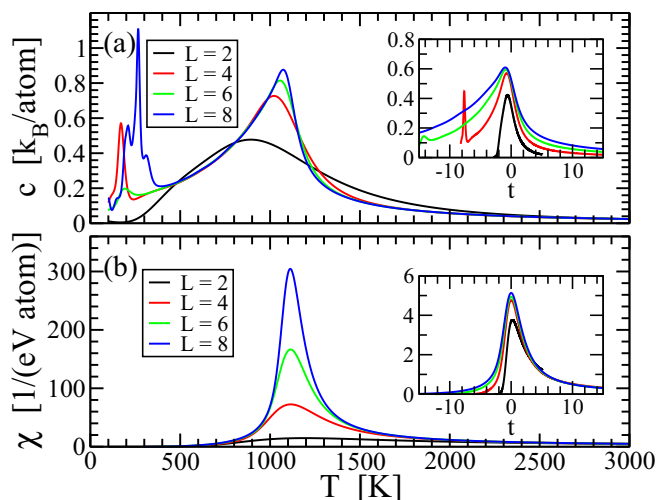


FIG. 7. Quaternary MoNbTaW. (a) Specific heat $c(T)$ and (b) susceptibility $\chi(T)$ vs temperature T for system sizes $L = 2$ (black), 4 (red), 6 (green), and 8 (blue). Insets show scaling functions as defined in text.

accuracy of the CVM entropy estimates closely resembles the binary case. The specific heat and susceptibility also show an Ising-like transition (Fig. 7), although at a lower critical temperature of $T_c \approx 1110$ K compared with the binary case. The lower critical temperature can be attributed to dilution of the strongly interacting MoTa pairs by the more weakly interacting Nb and W. Dilution is known to reduce T_c for Ising models [49], and a related frustration effect has been reported in high entropy alloys with varying numbers of components [23].

The strength of the Mo-Ta interaction may be due to the relatively strong variation in the electronegativity and atomic volume compared with Nb and W: for electronegativity χ_e (in Pauling units), $\text{Ta} (1.5) \lesssim \text{Nb} (1.6) \ll \text{Mo} (2.16) \lesssim \text{W} (2.36)$, and for atomic volume (in $\text{\AA}^3/\text{atom}$), $\text{Ta} (18.00) \gtrsim \text{Nb} (17.97) \gg \text{W} (15.85) \gtrsim \text{Mo} (15.55)$. Electronegativity differences create net charge transfer from group V elements (Nb and Ta) to group VI elements (Mo and W). See the Appendix for further discussion of the impact of electronegativity. Interaction strengths of elements in group V with elements in group VI range from 2 to 10 times stronger than among elements of the same group [12], with Mo-Ta being the strongest by nearly a factor of 2.

At temperatures below 300 K the quaternary undergoes a second transition [30] to a two-phase mixture of B2-type MoTa and B32-type NbW (see Fig. 8). Because the separated structure we obtain is no longer single phase, the CVM formulas do not apply. The specific heat and histogram entropy remain above zero, suggesting incomplete ordering at the lowest temperatures. The interface between the B2 and B32 phases is not sharp in Fig. 7(b), reflecting the high residual entropy and possibly indicating a lack of complete equilibration. Full first principles calculations predict a more complex low temperature structure consisting elemental Nb coexisting with a quaternary phase $\text{Mo}_2\text{NbTa}_2\text{W}_2$ Pearson type hR7 [12]. Our simple model does not capture this behavior accurately.

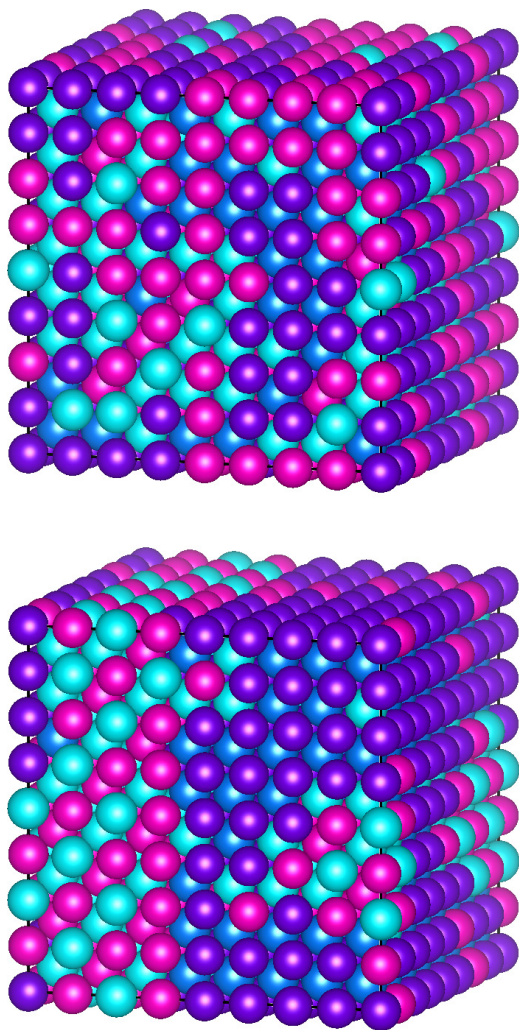


FIG. 8. $L = 8$ quaternary MoNbTaW at $T = 390$ K (top) showing the B2 phase and at $T = 100$ K (bottom) showing phase separation. The color scheme is chosen so that purple (Mo) and magenta (W) alternate with cyan (Nb) and blue (Ta) in the B2 phase. Lighter colors (NbW in the B32 structure) separate from dark colors (MoTa in the B2 structure) at low T .

IV. CONCLUSIONS

This work introduced an approach to modeling interatomic interactions based on a lookup table of precalculated cluster motifs. The interaction is quick to create from high throughput first principles total energy calculations. It can be readily generalized to a wide variety of high entropy alloys, and it scales as the factorial of the number of species employed but remains quite tractable up to five or six chemical species because the initial calculations are so fast and no subsequent fitting is required.

We applied the model to replica exchange Monte Carlo simulations that efficiently sample the equilibrium ensembles across a broad range of temperatures. The data accumulated during the simulation were analyzed using the multiple histogram method that reveals thermodynamic properties as continuous functions of temperature. We also took simulated cluster frequencies as input to directly evaluate the

entropy within the approximations of Kikuchi’s cluster variation method. If a Monte Carlo simulation was performed, the CVM formalism yielded entropy with almost no additional computational cost. In addition, thermodynamic integration is not required, so a simulation at a single temperature will directly reveal the entropy at that temperature. Our computational tools are available in the public domain [32].

Our use of the CVM entropy formulas differs from the usual application, where the energy and entropy models are combined to create a free energy functional whose minima yield cluster frequencies and other thermodynamic information. Although we could have done the same using our energy lookup table, the approach we take generalizes readily to full *ab initio* Monte Carlo and hybrid Monte Carlo/molecular dynamics, in which an energy model is not available. The usual CVM approach was applied to MoNbTaW [23], using an energy model with more precise values, and our results are largely consistent with the earlier one. Directly incorporating simulated cluster frequencies into the CVM entropy formulas was previously studied for simple model systems [27,28].

We carried out a high temperature series expansion for the bcc Ising model in order to analytically model the convergence of the CVM entropy formulas. We found that the tetrahedron approximation is exact through fourth order in inverse temperature, while pair and triangle approximations are exact only through second order, confirming the recommended site:NN:tetrahedron sequence of maximal clusters [26]. Lengthy simulations are required to obtain sufficient accuracy in the tetrahedron frequencies, so we suggest that

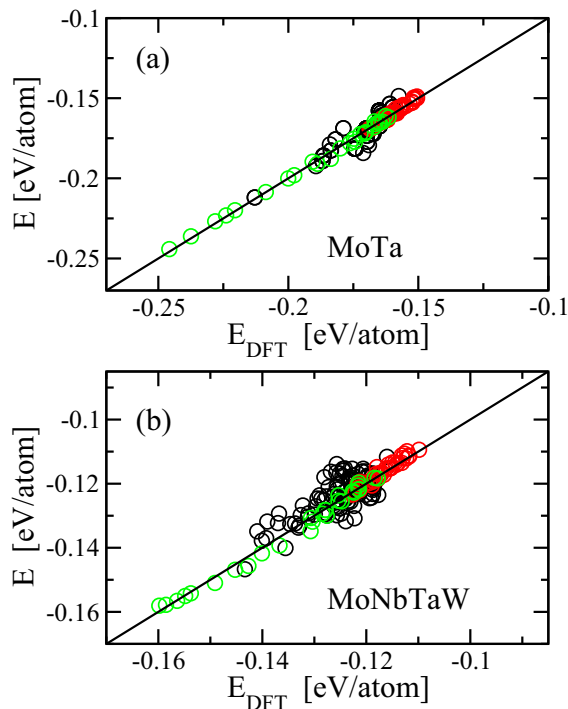


FIG. 9. Parity plot for tetrahedron plus polarization model energy/atom vs full DFT energy/atom for (a) MoTa and (b) MoNbTaW. All structures are equiatomic; black shows random 16-atom structures, red shows random 128-atom structures, and green shows MC-generated 128-atom structures.

stopping at the pair level (also known as the Bethe approximation [10,40,46]) should provide sufficient accuracy for most purposes.

The results of our simulation confirm that the A2 to B2 transition lies in the Ising universality class both for the binary MoTa and for the quaternary MoNbTaW. Our results for the temperature-dependent entropy show that despite the presence of short-range order above T_c , as revealed by the pair frequencies $y_{\alpha\gamma}$, the entropy loss is less than 20%, around $0.1k_B$ for MoTa and $0.2k_B$ for MoNbTaW. Below T_c , with the onset of symmetry breaking in the single-site occupation, the entropy drops rapidly.

ACKNOWLEDGMENTS

A.D.K. was supported by the SURF program at Carnegie Mellon University and by the National Science Foundation under Grant No. 2103958; M.W. was supported by the Department of Energy under Grant No. DE-SC0014506. We thank W. Al-Saidi and F. Koermann for useful discussions on interatomic interaction models.

APPENDIX: POLARIZATION CORRECTION

The skewing of tetrahedron model energies above parity with DFT requires discussion. Because our lookup table is

based on primitive cells of the cubic Heusler structure, every atom is in an environment of perfect cubic symmetry, while in a random structure most atoms are in environments of low symmetry. Anisotropic charge transfer can create local electric fields that will polarize the atoms. Hence, we propose a heuristic correction to the energy of the form

$$\Delta E = -\frac{|\mathbf{P}|^2}{2\chi_P}, \quad (\text{A1})$$

applied to each atom, where χ_P is an adjustable parameter that mimics dielectric susceptibility and the “polarization”

$$\mathbf{P} = \sum_{\mathbf{r}} \mathbf{r} \chi_e(\mathbf{r}) \quad (\text{A2})$$

is a measure of the anisotropy of Pauling’s electronegativity χ_e . Here \mathbf{r} is taken relative to the atom in question, and the sum extends over nearest neighbors ($|\mathbf{r}| = 1/\sqrt{2}$). This one-parameter correction results in improved agreement with a mean absolute error of 1 meV/atom relative to the full DFT energies for MoTa (setting $\chi_P = 125$) and 3 meV/atom for MoNbTaW (setting $\chi_P = 250$). Our success in removing the skew (see Fig. 9) suggests our explanation may possess some validity.

-
- [1] J.-W. Yeh, S.-K. Chen, S.-J. Lin, J.-Y. Gan, T.-S. Chin, T.-T. Shun, C.-H. Tsau, and S.-Y. Chang, *Adv. Eng. Mater.* **6**, 299 (2004).
- [2] B. Cantor, I. T. H. Chang, P. Knight, and A. J. B. Vincent, *Mater. Sci. Eng., A* **375–377**, 213 (2004).
- [3] O. N. Senkov, G. B. Wilks, D. B. Miracle, C. P. Chuang, and P. K. Liaw, *Intermetallics* **18**, 1758 (2010).
- [4] O. Senkov, J. Scott, S. Senkova, D. Miracle, and C. Woodward, *J. Alloys Compd.* **509**, 6043 (2011).
- [5] H. Yao, J. Qiao, J. Hawk, H. Zhou, M. Chen, and M. Gao, *J. Alloys Compd.* **696**, 1139 (2017).
- [6] J. Chen, X. Zhou, W. Wang, B. Liu, Y. Lv, W. Yang, D. Xu, and Y. Liu, *J. Alloys Compd.* **760**, 15 (2018).
- [7] D. Miracle and O. Senkov, *Acta Mater.* **122**, 448 (2017).
- [8] O. N. Senkov, D. B. Miracle, K. J. Chaput, and J.-P. Couzinie, *J. Mater. Res.* **33**, 3092 (2018).
- [9] E. P. George, D. Raabe, and R. O. Ritchie, *Nat. Rev. Mater.* **4**, 515 (2019).
- [10] D. de Fontaine, *Solid State Phys.* **34**, 73 (1979).
- [11] W. P. Huhn and M. Widom, *JOM* **65**, 1772 (2013).
- [12] M. Widom, in *High Entropy Alloys: Fundamentals and Applications* (Springer, Switzerland, 2015), Chap. 8, pp. 267–298.
- [13] M. C. Tropicovsky, J. R. Morris, P. R. C. Kent, A. R. Lupini, and G. M. Stocks, *Phys. Rev. X* **5**, 011041 (2015).
- [14] C. D. Woodgate and J. B. Staunton, *Phys. Rev. B* **105**, 115124 (2022).
- [15] M. Widom, W. Huhn, S. Maiti, and W. Steurer, *Metall. Mater. Trans. A* **45**, 196 (2014).
- [16] L. J. Santodonato, P. K. Liaw, R. R. Unocic, H. Bei, and J. R. Morris, *Nat. Commun.* **9**, 4520 (2018).
- [17] M. Widom, *Metall. Mater. Trans. A* **47**, 3306 (2016).
- [18] R. H. Swendsen and J.-S. Wang, *Phys. Rev. Lett.* **57**, 2607 (1986).
- [19] A. M. Ferrenberg and R. H. Swendsen, *Phys. Rev. Lett.* **61**, 2635 (1988).
- [20] A. M. Ferrenberg and R. H. Swendsen, *Phys. Rev. Lett.* **63**, 1195 (1989).
- [21] R. Kikuchi, *Phys. Rev.* **81**, 988 (1951).
- [22] H. Ackermann, G. Inden, and R. Kikuchi, *Acta Metall.* **37**, 1 (1989).
- [23] C. G. Schön, T. Duong, Y. Wang, and R. Arróyave, *Acta Mater.* **148**, 263 (2018).
- [24] J. Yeomans, *Statistical Physics of Fields* (Clarendon, Oxford, 1992).
- [25] M. Kardar, *Statistical Mechanics of Phase Transitions* (Cambridge Press, Cambridge, UK, 2007).
- [26] D. A. Vul and D. de Fontaine, *MRS Proc.* **291**, 401 (1992).
- [27] C. Bichara and G. Inden, in *Proceedings of the a NATO Advanced Study Institute on Statics and Dynamics of Alloy Phase Transformations* (Plenum Press, New York, 1994), pp. 541–544.
- [28] L. G. Ferreira, C. Wolverton, and A. Zunger, *J. Chem. Phys.* **108**, 2912 (1998).
- [29] A. Fernandez-Caballero, J. S. Wrobel, P. M. Mummery, and D. Nguyen-Manh, *J. Phase Equilib. Diffus.* **38**, 391 (2017).
- [30] T. Kostichenko, F. Koermann, J. Neugebauer, and A. Shapeev, *npj Comput. Mater.* **5**, 55 (2019).
- [31] Y. Ikeda, B. Grabowski, and F. Koermann, *Mater. Charact.* **147**, 464 (2019).
- [32] A. D. Kim and M. Widom, Replica Exchange Monte Carlo, <http://alloy.phys.cmu.edu/software/REMC/>.

- [33] N. Hoffman and M. Widom, *Metall. Mater. Trans. A* **52**, 1551 (2021).
- [34] G. Kresse and J. Furthmüller, *Phys. Rev. B* **54**, 11169 (1996).
- [35] G. Kresse and D. Joubert, *Phys. Rev. B* **59**, 1758 (1999).
- [36] J. P. Perdew, K. Burke, and M. Ernzerhof, *Phys. Rev. Lett.* **77**, 3865 (1996).
- [37] B. Feng and M. Widom, *Mater. Chem. Phys.* **210**, 309 (2018).
- [38] A. van de Walle, M. Asta, and G. Ceder, *CALPHAD: Comput. Coupling Phase Diagrams Thermochem.* **26**, 539 (2002).
- [39] A. M. Ferrenberg and R. H. Swendsen, *Comput. Phys.* **3**, 101 (1989).
- [40] J. S. Yedidia, W. T. Freeman, and Y. Weiss, *IEEE Trans. Inf. Theory* **51**, 2282 (2005).
- [41] A. Pelizzola, *J. Phys. A* **38**, R309 (2005).
- [42] W. L. Bragg and E. J. Williams, *Proc. R. Soc. London, Ser. A* **145**, 699 (1934).
- [43] G. F. Newell and E. W. Montroll, *Rev. Mod. Phys.* **25**, 353 (1953).
- [44] G. A. Baker, *Phys. Rev.* **129**, 99 (1963).
- [45] J. Pearl, *Probabilistic Reasoning in Intelligent Systems: Networks of Plausible Inference* (Morgan Kaufmann, San Francisco, 1988).
- [46] J. Yedidia, in *Advanced Mean Field Methods: Theory and Practice*, edited by M. Opper and D. Saad (MIT Press, Cambridge, MA, 2001), Chap. 3, pp. 21–36.
- [47] D. Landau and K. Binder, *A Guide to Monte Carlo Simulations in Statistical Physics* (Cambridge Press, Cambridge, UK, 2005).
- [48] A. Pelissetto and E. Vicari, *Phys. Rep.* **368**, 549 (2002).
- [49] C. Jayaprakash, E. K. Riedel, and M. Wortis, *Phys. Rev. B* **18**, 2244 (1978).